12^{th} International Conference on Fracture Mechanics of Concrete and Concrete Structures
FraMCoS-12
B.L.A. Pichler, Ch. Hellmich, P. Preinstorfer (Eds)

https://doi.org/10.21012/FC12.1344
TT-C1:2

COMPARATIVE ANALYSIS OF 2D AND 3D MESOSCOPIC SIMULATIONS OF AN ACCELERATED REBAR CORROSION TEST

Yue Li[*†], Xin Ruan[†], Herbert A. Mang[*†], and Bernhard Pichler[*]

[*] Institute for Mechanics of Materials and Structures, TU Wien (Vienna University of Technology)
Vienna, Austria, European Union
e-mail: yue.li@tuwien.ac.at

[†] College of Civil Engineering, Tongji University
Shanghai, China

Key words: Accelerated rebar corrosion test, Mesoscopic simulation, 2D simplification, Comparative analysis

Abstract. Two-dimensional (2D) mesoscopic simulations of accelerated corrosion tests are frequently performed to avoid the much higher computational costs of three-dimensional (3D) mesoscopic simulations. 2D models assume geometric invariance of the mesostructure in the direction perpendicular to the analyzed plane. However, this is different from the real concrete mesostructure, consisting of polyhedral (rather than cylindrical) aggregate particles embedded in a mortar matrix. This provides the motivation for a comparative analysis of 2D and 3D mesoscopic simulations of the accelerated rebar corrosion test by Andrade et al. [Mat. Struct., 1993, 453-464]. The 3D model resolves the concrete mesostructure in the vicinity of the rebar into polyhedral aggregates, embedded in the mortar matrix. The 3D simulation accounts for non-uniform corrosion penetration into the rebar, non-uniform rust deposition on the rebar surface, and crack propagation through the mesostructure of concrete. Four 2D models are generated from four different cross-sections through the 3D model, perpendicular to the axis of the rebar. The 2D simulations are based on the assumption of either a plane strain state or a plane stress state. The comparison of the results of 2D and 3D simulations indicates that the 2D simplification does not necessarily result in the realistic simulation of the interaction of propagating cracks with the aggregates. This may lead to wrong predictions of crack propagation paths and crack opening widths.

1 INTRODUCTION

Corrosion-induced cracking is one of the most common types of deterioration of reinforced concrete structures. Mesostructural features of concrete govern the non-uniform corrosion of the rebars and crack propagation through the concrete cover. Both processes have been investigated by means of accelerated rebar corrosion tests. Mesostructural changes were documented e.g. by means of X-ray computed tomography [1] and microscopic imaging of polished specimen cross-sections [2], respectively.

Numerical simulations, especially mesoscopic simulations, provide valuable additional insight into the mechanisms responsible for corrosion-induced cracking. Such simulations resolve the mesostructure of con-

crete into aggregate particles which are separated from the surrounding mortar matrix by some 20 µm-thick interfacial transition zones (ITZs). The heterogeneity of concrete is taken into account when computing the non-uniform current density, the corrosion reaction, and the rust deposition on the steel-concrete interface (SCI) [3]. On the one hand, this allows for reproduction of crack propagation through the concrete cover as observed in accelerated rebar corrosion tests. On the other hand, the fine discretization with finite elements, which is required for the detailed resolution of the mesostructure of concrete, results in considerable computational demands.

2D simplifications are, therefore, widely used in mesoscopic simulations of accelerated rebar corrosion tests to reduce computational costs [4]. Such simulations assume the geometrical invariance of the mesostructure in the direction perpendicular to the analyzed plane. However, this assumption deviates from the actual 3D mesostructure of concrete which consists of polyhedral (rather than cylindrical) aggregates embedded in the mortar matrix. This provides the motivation to perform 2D *and* 3D simulations and compare the results. The present study is conducted on the basis of a 3D model [5] which reproduces the results of the accelerated rebar corrosion test by Andrade et al. [6]. Four 2D models are generated from four different cross-sections through the 3D model. By comparing the results of the 2D and the 3D simulations, this study reveals the potential and the limitations of 2D mesoscopic simulation models.

Along this line, the paper is organized as follows: Section 2 contains data from the test by Andrade et al. [6]. Section 3 contains the description of the 3D and 2D models. In Section 4, results of the 3D and 2D simulations are compared. The differences are discussed in Section 5. This includes differences of 2D simulations performed under the assumption of either a plane stress state or a plain strain state. Finally, the conclusions of the study are presented in Section 6.

2 ACCELERATED CORROSION TEST BY ANDRADE ET AL. [6]

The analyzed test was performed by Andrade et al. [6] on a cubical reinforced concrete specimen with the dimensions of 150 mm × 150 mm × 380 mm. A 16 mm-diameter ordinary corrugated steel rebar was embedded parallel to the longest axis of the specimen. The concrete covers on the top and the right sides of the rebar were equal to 2 cm and 3 cm, respectively, see Fig. 1(a).

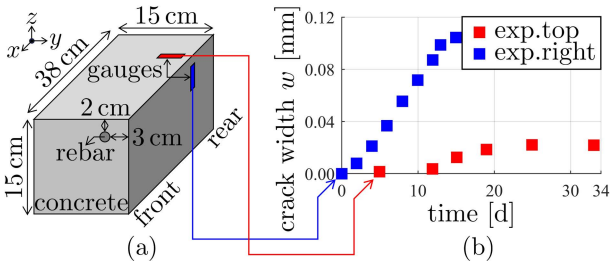

Figure 1: Accelerated corrosion test by Andrade et al. [6]: (a) layout of the specimen and (b) measured evolution of crack opening widths.

An electric current was imposed in the 34-day test on the rebar by an ordinary galvanostat. The prescribed average current density amounted to 100 µA/cm^2 along the SCI. The counter electrode was placed underneath the specimen.

The first crack was observed in the rear half of the specimen, at the right lateral surface, at the height of the rebar, running virtually parallel to it, see the blue symbols indexed "exp.right" in Fig. 1(b). Later, a second crack was observed on the top surface, see the red symbols indexed "exp.top" in Fig. 1(b). The opening of this second crack was always significantly smaller than that of the first crack.

3 FINITE ELEMENT MODELS

3.1 3D model

The 3D finite element model is taken from [5]. Denoted as "M3", it was developed with the purpose of reproducing the cracking of the specimen. The dimensions of the discretized domain are 150 mm × 150 mm × 50 mm. The model refers to the rear-end section of the analyzed specimen, see Fig. 2. The rebar is represented by a cylinder. Its radius, r, is equal to 8 mm. Its length, L, is equal to 50 mm. Its distances from the top surface and the right surface of the model are the same as the ones between the rebar and the corresponding surfaces of the specimen. In the quarter of the model around the rebar, the mesostructure of the concrete is resolved into polyhedral coarse aggregates, with characteristic sizes larger than 5 mm, embedded in the mortar matrix, see also Fig. 2. In the other three quarters of the model, the concrete is represented as a homogeneous material to save modeling and computational efforts. Stresses due to gravity are disregarded.

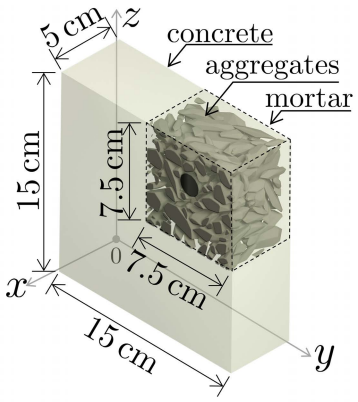

Figure 2: 3D finite element model.

The mechanical properties of the concrete, the mortar matrix, the aggregates, and the ITZs are upscaled using the Mori-Tanaka scheme of continuum micromechanics [7, 8], or taken from the literature [3, 6, 9, 10], see Table 1. In the region where the finite element model resolves the mesostructure of the concrete, the influence of segregation of the fresh mortar from both the rebar and the coarse aggregates is considered explicitly: a semi-elliptical porous zone with a maximum thickness of 20 µm is introduced underneath the rebar. The modulus of elasticity of the ITZ is smaller on the under-sides of the aggregates than on their top-sides, see also Table 1.

Positions on the corroding rebar surface are described with cylindrical coordinates. The axial coordinate, l, ranges in the interval $[0,\, L]$. The azimuth angle, θ, ranges in the interval $[0,\, 2\pi]$, see Fig. 3.

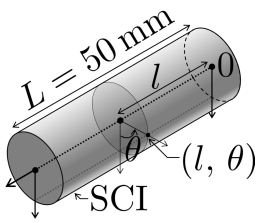

Figure 3: Cylindrical coordinates describing the position at the SCI.

The dissolution of iron from the rebar surface is driven by the imposed current, following the macrocell corrosion mechanism [11]. According to Faraday's law [12], the inward corrosion penetration at point (l, θ) and at time t, i.e. $\boldsymbol{u}_{\mathrm{c}}(l, \theta, t)$, is proportional to the time integral of the local current density $\boldsymbol{i}(l, \theta, t)$:

$$\boldsymbol{u}_{\mathrm{c}}(l,\theta,t) = -\frac{A_{\mathrm{s}} \int_0^t |\boldsymbol{i}(l,\theta,t)| \mathrm{d}t}{\rho_{\mathrm{s}} F z_{\mathrm{Fe}}} \boldsymbol{n}_{\mathrm{SCI}}(l,\theta)\,, \tag{1}$$

where $A_{\mathrm{s}} = 55.85\,\mathrm{g/mol}$ is the molar mass of steel, $\boldsymbol{n}_{\mathrm{SCI}}(l, \theta)$ is the unit vector at point (l, θ), normal to the SCI, pointing from the surface of the steel rebar into the concrete phase, $\rho_{\mathrm{s}} = 7.8\,\mathrm{g/mm^3}$ is the mass density of steel, $F = 9.65 \times 10^4\,\mathrm{C/mol}$ is Faraday's constant, and $z_{\mathrm{Fe}} = 2$ is the valence of the anodic reaction. The volume of dissolved iron, $V_{\mathrm{c}}(t)$, is obtained from integration of

Table 1: Mechanical properties of concrete and of its constituents, obtained by means of up-scaling [7,8] or taken from the literature [3,6,9,10].

properties	E	ν	σ_{ts}	G_{f}
unit	[GPa]	[–]	[MPa]	[J/m^2]
concrete	33.52	0.21	3.55	95
mortar	26.09	0.22	4.00	60
aggregate	50.00	0.20	8.00	>200
ITZ on the top-sides of the aggregates	11.65	0.23	2.50	30
ITZ on the under-sides of the aggregates	10.21	0.23	2.50	30

E: modulus of elasticity; ν: Poisson's ratio; σ_{ts}: tensile strength; G_{f}: fracture energy.

$|\boldsymbol{u}_{\mathrm{c}}(l,\theta,t)|$ over the rebar surface:

$$V_{\mathrm{c}}(t) = \int_0^L \int_0^{2\pi} |\boldsymbol{u}_{\mathrm{c}}(l,\theta,t)|\, r \, \mathrm{d}\theta \, \mathrm{d}l \,. \tag{2}$$

The current density on the SCI, $\boldsymbol{i}$, is (according to Ohm's law [13]) proportional to the gradient of the electric potential ϕ:

$$\boldsymbol{i} = -\gamma \nabla \phi \,, \tag{3}$$

where ∇ is the gradient operator; γ stands for the homogenized electric conductivity. The electric conductivity of concrete and mortar are quantified with the Maxwell Garnett model [14] as 6.7×10^{-3} S/m and 13.2×10^{-3} S/m, respectively.

The dissolution of iron produces ferrous (Fe^{2+}) and ferric (Fe^{3+}) ions [15]. They precipitate out of the oversaturated pore water solution as rust partly at the location where the steel rebar was dissolved and partly in the pores of the concrete [16]. The volume of the portion resulting in an outward movement of the SCI, V_{r}, is around 1.44 times the volume of the dissolved iron, see $V_{\mathrm{c}}(t)$ in Eq. (2), according to the measurement by Caré et al. [17] and numerical analysis in [5]:

$$V_{\mathrm{r}}(t) = 1.44\, V_{\mathrm{c}}(t) \,. \tag{4}$$

The non-uniform outward movement of the SCI around the rebar is denoted as $\boldsymbol{u}_{\mathrm{r}}(l,\theta,t)$. It is modeled as a two-stage process:

$$\boldsymbol{u}_{\mathrm{r}}(l,\theta,t) = \begin{cases} \boldsymbol{u}_{\mathrm{r,s1}}(l,\theta,t) \,, & t \le t^* \,, \\ \boldsymbol{u}_{\mathrm{r,s2}}(l,\theta,t) \,, & t > t^* \,. \end{cases} \tag{5}$$

In stage 1, where $t \le t^*$, the precipitation of rust fills the segregation-induced semi-elliptical porous zone underneath the rebar. The corresponding outward movement of the SCI, $\boldsymbol{u}_{\mathrm{r,s1}}$, reads as

$$\boldsymbol{u}_{\mathrm{r,s1}}(l,\theta,t) = h_{\mathrm{r}}(\theta,t)\, \boldsymbol{n}_{\mathrm{SCI}}(l,\theta) \,, \quad t \le t^*, \tag{6}$$

where $h_{\mathrm{r}}(\theta,t)$ is the position- and time-dependent thickness of the rust layer formed inside the semi-elliptical domain underneath the rebar, see Fig. 4, i.e.

$$h_{\mathrm{r}}(\theta,t) = \frac{r^2 + r\, h_{\mathrm{r0}}(t)}{\sqrt{(r + h_{\mathrm{r0}}(t))^2 \sin^2\theta + r^2 \cos^2\theta}} - r \tag{7}$$

for $|\theta| \le \pi/2$; and $h_{\mathrm{r}}(\theta,t) = 0$ for $|\theta| > \pi/2$.

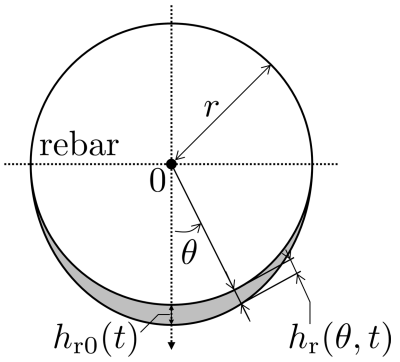

Figure 4: Illustration of the semi-elliptical outward movement of the SCI at stage 1.

In Eq. (7), $h_{\mathrm{r0}}(t)$ is defined as

$$h_{\mathrm{r0}}(t) = \frac{2\, V_{\mathrm{r}}(t)}{\pi\, r\, L} \,. \tag{8}$$

The transition time t^* is reached, once the segregation-induced semi-elliptical porous zone underneath the rebar is completely filled by rust. This means that the maximum outward movement, $h_{\mathrm{r0}}(t^*)$, is equal to the maximum thickness of the semi-elliptical zone, $h_{\mathrm{r0,max}} = 20\,\mu\mathrm{m}$, see [18].

In stage 2, where $t > t^*$, the additional outward movement of the SCI is 1.44 times the non-uniform increase of the inward corrosion penetration into the rebar:

$$\begin{aligned}\boldsymbol{u}_{\mathrm{r,s2}}(l,\theta,t) &= h_{\mathrm{r}}\,(\theta,t^*)\,\boldsymbol{n}_{\mathrm{SCI}}(l,\theta)\\ &\quad - 1.44[\boldsymbol{u}_{\mathrm{c}}(l,\theta,t) - \boldsymbol{u}_{\mathrm{c}}(l,\theta,t^*)]\,, \quad t > t^*\,.\end{aligned} \tag{9}$$

Cracking of concrete is simulated by means of continuum damage mechanics. A scalar damage variable, d, is introduced to describe the deterioration of the isotropic elastic stiffness in the stress-strain relationship

$$\boldsymbol{\sigma} = (1-d)\,\mathbb{C} : \boldsymbol{\varepsilon}\,, \tag{10}$$

where $\boldsymbol{\sigma}$ is Cauchy's stress tensor, $\mathbb{C}$ is the fourth-order elasticity tensor describing the initial (undamaged) elastic stiffness of the material, $\boldsymbol{\varepsilon}$ is the linearized strain tensor, and ":" stands for the double contraction tensor product.

Adopting exponential strain softening [19], the evolution of d is related to the maximum κ of the largest principal strains ε_1 experienced by the material:

$$d(\kappa) = \begin{cases} 0\,, & \kappa \le \varepsilon_{\mathrm{cr}}\,,\\ 1 - \dfrac{\varepsilon_{\mathrm{cr}}}{\kappa}\exp\left(-\dfrac{\kappa-\varepsilon_{\mathrm{cr}}}{\varepsilon_{\mathrm{f}}-\varepsilon_{\mathrm{cr}}}\right)\,, & \kappa > \varepsilon_{\mathrm{cr}}\,, \end{cases} \tag{11}$$

where $\varepsilon_{\mathrm{cr}}$ denotes the elastic strain at the onset of damage due to uniaxial tension, calculated from the tensile strength, σ_{ts}, and the modulus of elasticity, E, of the intact (undamaged) concrete as

$$\varepsilon_{\mathrm{cr}} = \frac{\sigma_{\mathrm{ts}}}{E}\,. \tag{12}$$

The strain-softening regime is described by

$$\varepsilon_{\mathrm{f}} = \frac{G_{\mathrm{f}}}{\sigma_{\mathrm{ts}}\,l_{\mathrm{FE}}} + \varepsilon_{\mathrm{cr}}\,, \tag{13}$$

where ε_{f} stands for a strain-like parameter. In Eq. (13), G_{f} denotes the amount of energy dissipated per unit area of cracking during strain localization, see also Table 1, and l_{FE} stands for the element size, given as

$$l_{\mathrm{FE}} = \sqrt[3]{6\sqrt{2}V_{\mathrm{FE}}}\,, \tag{14}$$

where V_{FE} denotes the volume of 3D finite elements. According to Rots et al. [20], the crack width, w, in the concrete and the mortar is quantified as

$$w = \begin{cases} 0\,, & \varepsilon_1 \le \varepsilon_{\mathrm{cr}}\,,\\ l_{\mathrm{FE}}\,\varepsilon_1\,, & \varepsilon_1 > \varepsilon_{\mathrm{cr}}\,, \end{cases} \tag{15}$$

where ε_1 is the largest principal tensile strain.

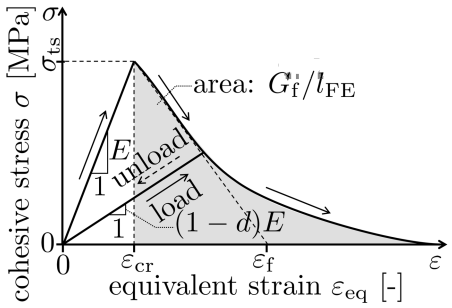

Figure 5: Illustration of the stress-strain relation during exponential strain softening.

3.2 2D models

Four 2D finite element models are generated by cutting the 3D finite element model perpendicular to the axis of the rebar at positions $l_1 = 1.0\,\mathrm{cm}$, $l_2 = 2.0\,\mathrm{cm}$, $l_3 = 3.0\,\mathrm{cm}$, and $l_4 = 4.0\,\mathrm{cm}$, see Fig. 6. The dimensions of the 2D models are $150\,\mathrm{mm} \times 150\,\mathrm{mm}$. The circle with a radius of 8 mm on the top-right of the models represents the rebar. The quarter of the model around the rebar is resolved into polygonal coarse aggregates, covered by the ITZ layer and embedded in the mortar matrix. In the other three quarters, the concrete is represented as a homogeneous material. The mechanical properties of the concrete, the mortar matrix, the aggregates, and the ITZs are the same as before, see Table 1.

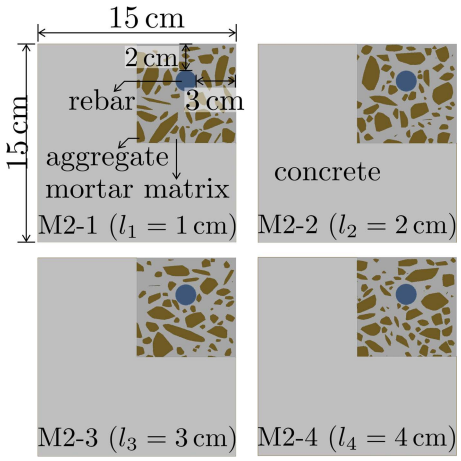

Figure 6: Four 2D finite element models obtained from cutting the 3D model.

The corrosion penetration into the rebar is computed for all four cross-sections according to Eq. (1), yielding $\boldsymbol{u}_\mathrm{c}(l_i, \theta, t)$ with $i = 1, 2, 3, 4$. The area of the dissolved iron, S_c, is quantified by analogy to Eq. (2) as

$$S_\mathrm{c}(l_i, t) = \int_0^{2\pi} |\boldsymbol{u}_\mathrm{c}(l_i, \theta, t)| \; r \, \mathrm{d}\theta \,. \tag{16}$$

The outward movement of the SCI, $\boldsymbol{u}_\mathrm{r}(l_i, \theta, t)$, is computed according to the Eqs. (5), (6), and (9). The area of the part of rust resulting in the outward movement of the SCI, S_r, is quantified according to Eq. (4) as

$$S_\mathrm{r}(l_i, t) = 1.44 \, S_\mathrm{c}(l_i, t) \,. \tag{17}$$

$h_\mathrm{r0}(l_i, t)$, see Eq. (8), is proportional to $S_\mathrm{r}(l_i, t)$:

$$h_\mathrm{r0}(l_i, t) = \frac{2 S_\mathrm{r}(l_i, t)}{\pi \, r} \,. \tag{18}$$

The mechanical behavior of concrete, of mortar, and of the ITZ in the 2D models is simulated in the same way as in the 3D model. Only the calculation of the characteristic size of finite elements is changed to

$$l_\mathrm{FE} = \sqrt{2 \, S_\mathrm{FE}} \,, \tag{19}$$

where S_FE denotes the area of the 2D finite elements. At first, the 2D simulations are based on the assumption of a plane strain state, which is commonly used [21]. Thus, the constitutive equations read as

$$\begin{aligned}
\sigma_{xx} &= \frac{(1-d)E}{(1+\nu)(1-2\nu)} [(1-\nu)\varepsilon_{xx} + \nu \varepsilon_{yy}] \,, \\
\sigma_{yy} &= \frac{(1-d)E}{(1+\nu)(1-2\nu)} [\nu \varepsilon_{xx} + (1-\nu)\varepsilon_{yy}] \,, \\
\sigma_{zz} &= \frac{E\nu}{(1+\nu)(1-2\nu)} (\varepsilon_{xx} + \varepsilon_{yy}) \,, \\
\sigma_{xy} &= \frac{(1-d)E}{1+\nu} \varepsilon_{xy} \,, \qquad \sigma_{yz} = \sigma_{zx} = 0 \,.
\end{aligned} \tag{20}$$

4 COMPARISON OF RESULTS OF THE 3D AND 2D MODELS

4.1 Current density in the concrete and along the rebar surface

Both in the 3D model and the 2D models the current flow lines start from the rebar surface, where the current is imposed. They are obstructed by the coarse aggregates, and they end at the bottom of the model, where the cathode is placed, see Fig. 7. The four different 2D models yield different distributions of current flow lines, influenced by the specific arrangement of the coarse aggregates in the vicinity of the rebar.

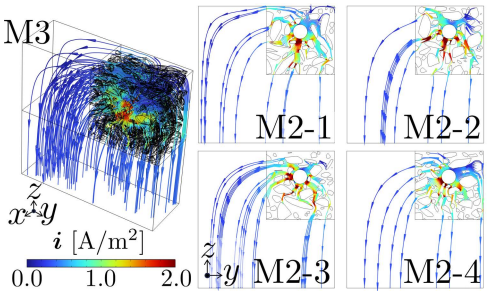

Figure 7: Distribution of the current density obtained from the 3D model and the 2D models.

The current density along the rebar surface varies in the 3D simulation with the azimuth angle, θ, and the axial coordinate, l, see the gray circles in Fig. 8. The current density is larger and more variable in the lower-left region of the rebar, reaching

a maximum value of 2.46 A/m^2. It is much smaller and less variable in the upper-right region, where the maximum value is equal to 0.69 A/m^2. The four different 2D models yield different distributions of the current density around the rebar, see the four blue lines in Fig. 8. For almost all values of θ inside $[0, 2\pi]$ the magnitude of the current density obtained from the 2D models is inside the interval of the magnitude of the current density obtained from the 3D model for this azimuth angle.

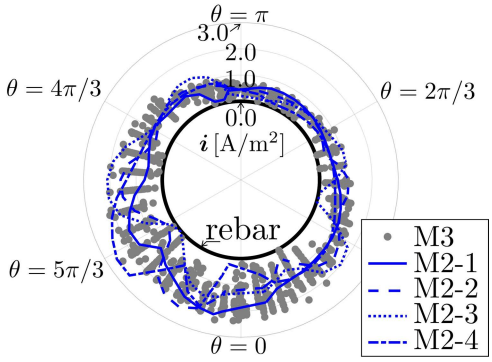

Figure 8: Distribution of the current density around the rebar surface obtained from the 3D model and the 2D models.

Therefore, the results of the four 2D models are consistent with those of the 3D model with respect to the current density. The large variability of the results indicates the strong influence of the distribution of the coarse aggregates around the rebar. This underscores the necessity of performing *several* 2D simulations with *different* realistic aggregate arrangements.

4.2 Corrosion penetration into the rebar

The corrosion penetration into the rebar surface at the end of the test, i.e. at $t = 34$ d, varies in the 3D simulation with both the azimuth angle, θ, and the axial coordinate, l, see the gray circles in Fig. 9. The corrosion penetration is larger and more variable in the lower-left region of the rebar, reaching a maximum value of 212 µm, while it is much smaller and less variable in the upper-right region, where the maximum value is equal to 57 µm. The four different 2D models yield different distributions of the corrosion penetration around the rebar, see the four blue lines in Fig. 9. Again, the variability of the results obtained from the four different 2D simulations is representative of the variability of the results obtained from the 3D simulation.

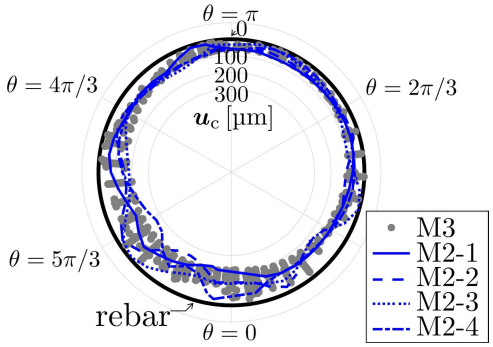

Figure 9: Distribution of the corrosion penetration into the rebar obtained from the 3D model and the 2D models.

4.3 Outward movement of the SCI, caused by the non-uniform deposition of the rust

The distribution of the outward movement of the SCI at the end of the test, i.e. at $t = 34$ d, varies in the 3D simulation with both the azimuth angle, θ, and the axial coordinate, l, see the gray circles in Fig. 10.

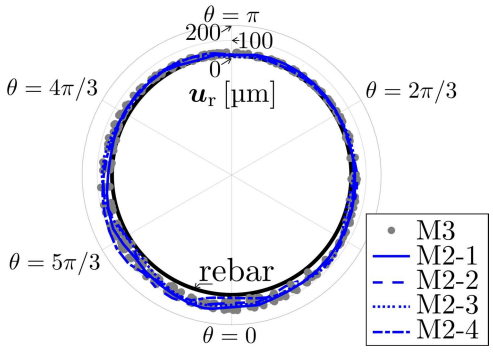

Figure 10: Distribution of the outward movement of the SCI obtained from the 3D model and the 2D models.

The magnitude and the variability are larger in the lower-left region of the rebar than elsewhere. Again, the variability of the results obtained from the four different 2D simulations, see the blue lines in Fig. 10, is representative of the variability of the results obtained from the 3D simulation.

4.4 Crack propagation through the concrete cover

In the 3D model the crack propagates to the right lateral surface of the concrete, see Fig. 11. This agrees with the experimental observation [6]. Only two 2D models, M2-3 and M2-4, resulted in qualitatively similar results, i.e. in concrete cracking toward the right lateral surface of the structure. The other two models, M2-1 and M2-2, resulted in concrete cracking toward the top surface of the concrete. This is qualitatively different from the results of the 3D simulation and from the observation in the accelerated corrosion test [6].

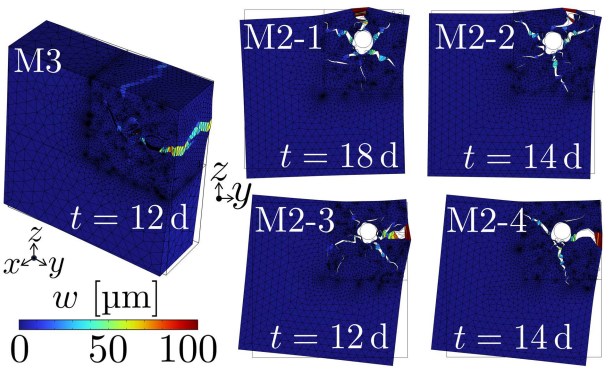

Figure 11: Distribution of the crack propagation path obtained from the 3D model and the 2D models.

The evolutions of the crack widths at the surfaces of the structure obtained from the 3D model, see the thick solid lines in Fig. 12, agree well with the test results by Andrade et al. [6], see the squares in Fig. 12. The evolutions of the crack widths obtained from the 2D models M2-1 and M2-2, see the solid and the dashed lines in Fig. 12, are different from those obtained from the 3D model. The other two 2D models, see the dotted and the dash-dotted lines in Fig. 12, delivered qualitatively and quantitatively reliable results.

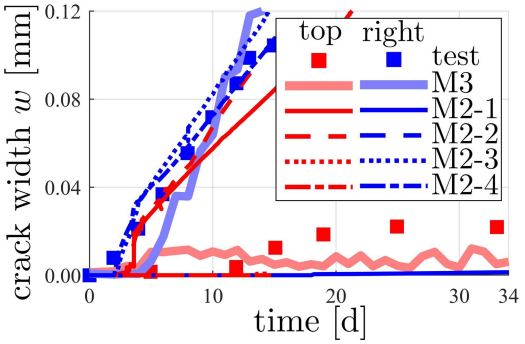

Figure 12: Evolutions of the crack widths on the top and the right surface of the test specimen [6], obtained from the 3D model and the 2D models.

5 DISCUSSION

5.1 Differences between the results of the 2D simulations and the result for the corresponding cross-sections obtained from the 3D simulation

Herein, the results of the 2D models are compared with the results of the 3D model obtained in the corresponding cross-sections at $l_1 = 1.0\,\text{cm}$, $l_2 = 2.0\,\text{cm}$, $l_3 = 3.0\,\text{cm}$, and $l_4 = 4.0\,\text{cm}$. The latter are labeled as M3-1, M3-2, M3-3, and M3-4, respectively.

The distributions of the current density around the rebar surface obtained from the 2D models are similar to those obtained from the corresponding cross-sections of the 3D model, see Fig. 13. Generally, they are largest in the lower-left region of the rebar. The aggregates positioned close to the rebar surface reduce the local current density significantly. Even "almost vanishing" values of the current density are found in the 3D and 2D models. To quantify the differences, the deviation $\delta \boldsymbol{i}$ is calculated as

$$\delta \boldsymbol{i}_i = \frac{\int_0^{2\pi} |\boldsymbol{i}_{3\text{D}}(l_i,\theta,t) - \boldsymbol{i}_{2\text{D}}(l_i,\theta,t)| r \mathrm{d}\theta}{\int_0^{2\pi} |\boldsymbol{i}_{3\text{D}}(l_i,\theta,t)| r \mathrm{d}\theta}\,, \tag{21}$$

where $\boldsymbol{i}_{3D}$ and $\boldsymbol{i}_{2D}$ denote the current density at the rebar surface obtained from the 3D model and the 2D models, respectively. Inserting $t = 34\,\mathrm{d}$ as well as $l_1 = 1\,\mathrm{cm}$, $l_2 = 2\,\mathrm{cm}$, $l_3 = 3\,\mathrm{cm}$, and $l_4 = 4\,\mathrm{cm}$, respectively, into Eq. (21) yields $\delta\boldsymbol{i}_1 = 0.24$, $\delta\boldsymbol{i}_2 = 0.35$, $\delta\boldsymbol{i}_3 = 0.17$, and $\delta\boldsymbol{i}_4 = 0.18$, respectively, as the values of the deviation for the four cross-sections. Thus, the distributions of the current density around the rebar obtained from the 2D models agree well with the result of the 3D model.

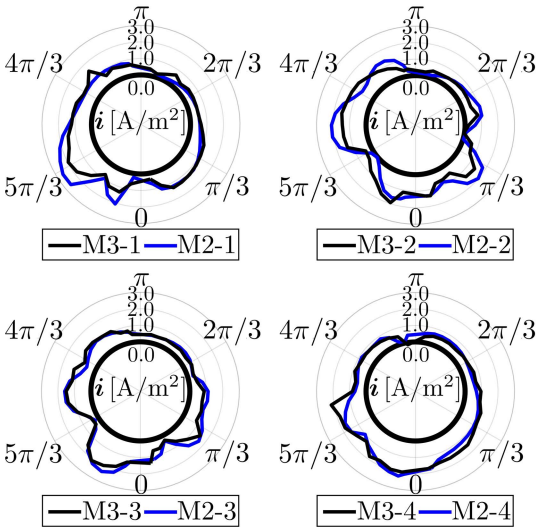

Figure 13: Distribution of the current density obtained from the 2D models and the corresponding cross-sections of the 3D model.

The distributions of the corrosion penetration into the rebar, at $t = 34\,\mathrm{d}$, obtained from the 2D models are close to the distributions at the corresponding cross-sections of the 3D model, see Fig. 14. Replacing $\boldsymbol{i}$ in Eq. (21) by $\boldsymbol{u}_c$, the deviations are quantified as $\delta\boldsymbol{u}_{c1} = 0.20$, $\delta\boldsymbol{u}_{c2} = 0.31$, $\delta\boldsymbol{u}_{c3} = 0.26$, and $\delta\boldsymbol{u}_{c4} = 0.13$, respectively, for the four cross-sections. Thus, the distributions of the corrosion penetration into the rebar obtained from the 2D models agree well with the result of the 3D model.

The distributions of the outward movement of the SCI, at $t = 34\,\mathrm{d}$, obtained from the 2D models are close to the distributions at the corresponding cross-sections of the 3D model, see Fig. 15. Replacing $\boldsymbol{i}$ in Eq. (21) by $\boldsymbol{u}_r$, the deviations are quantified as $\delta\boldsymbol{u}_{r1} = 0.20$, $\delta\boldsymbol{u}_{r2} = 0.29$, $\delta\boldsymbol{u}_{r3} = 0.26$, and $\delta\boldsymbol{u}_{r4} = 0.13$, respectively, for the four cross-sections. Thus, the distributions of the outward movement of the SCI obtained from the 2D models agree well with the result of the 3D model.

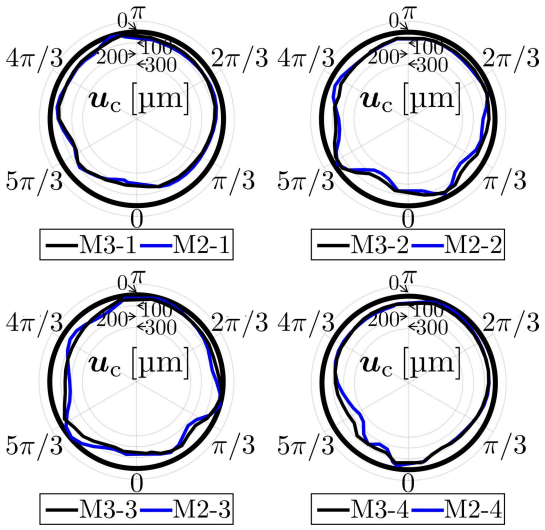

Figure 14: Distribution of the corrosion penetration into the rebar obtained from the 2D models and the corresponding cross-sections of the 3D model.

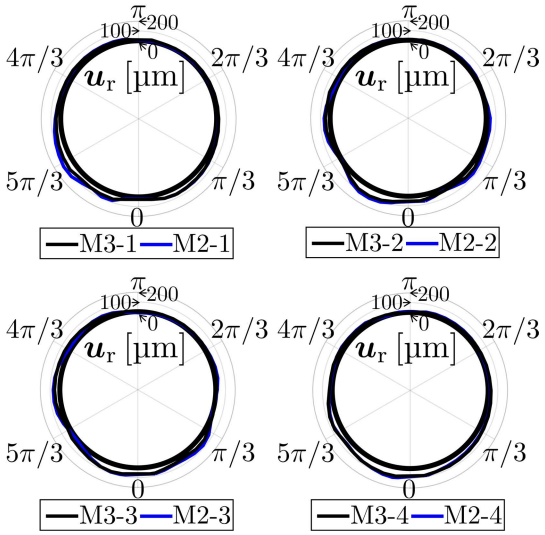

Figure 15: Distribution of the outward movement of the SCI obtained from the 2D models and the corresponding cross-sections of the 3D model.

The evolutions of the crack opening widths at the surfaces obtained from the 2D models are compared with the evolutions at the corresponding cross-sections of the 3D model, see Fig. 16. The results of the 2D model M2-3 agree well with the 3D results M3-3, and the results of the 2D model M2-4 agree well with the 3D results M3-4. However, the results of the 2D model M2-1 differ significantly from the 3D results M3-1, and the results of the 2D model M2-2 differ significantly from the 3D results M3-2, although the agreement regarding the outward movement of the SCI is satisfactory, see Fig. 15. Thus, the interaction of propagating cracks with the aggregates is not necessarily reproduced well in 2D models.

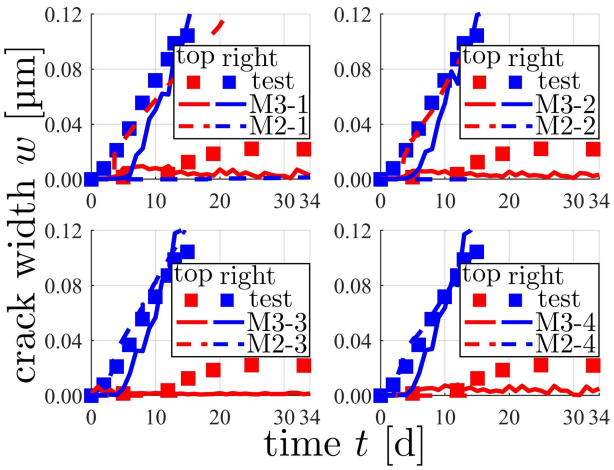

Figure 16: Evolutions of the crack widths at the surfaces of the concrete obtained from the 2D models and the corresponding cross-sections of the 3D model.

5.2 2D models based on the assumption of plane stress states

The 2D finite element simulations are repeated under the assumption of a plane stress state (rather than a plane strain state). Thus, the constitutive equations in Eq. (20) are replaced by

$$\begin{aligned}
\sigma_{xx} &= \frac{(1-d)E}{1-\nu^2}(\varepsilon_{xx}+\nu\varepsilon_{yy})\,,\\
\sigma_{yy} &= \frac{(1-d)E}{1-\nu^2}(\nu\varepsilon_{xx}+\varepsilon_{yy})\,,\\
\sigma_{xy} &= \frac{(1-d)E}{1+\nu}\varepsilon_{xy}\,,\\
\sigma_{xz} &= \sigma_{yz} = \sigma_{zz} = 0\,.
\end{aligned} \tag{22}$$

The evolutions of the crack opening widths at the surfaces obtained from the 2D models are compared with the evolutions at the corresponding cross-sections of the 3D model, see Fig. 17. The results of the 2D model M2-3 agree well with the 3D results M3-3, and the results of the 2D model M2-4 agree well with the 3D results M3-4. However, the results of the 2D model M2-1 differ significantly from the 3D results M3-1, and the results of the 2D model M2-2 differ significantly from the 3D results M3-2. Therefore, the assumption of a plane stress state instead of a plane strain state has no great influence on the simulation results.

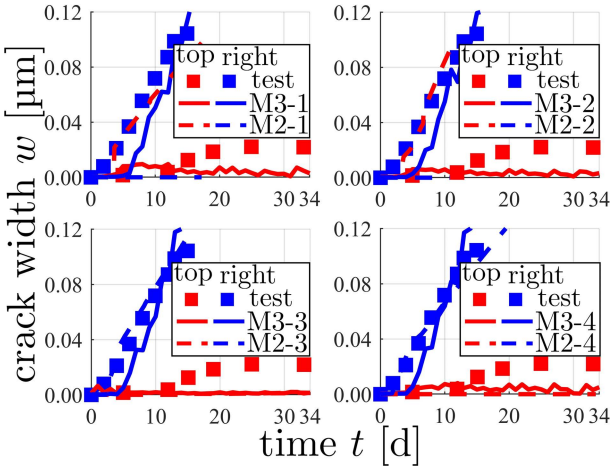

Figure 17: Evolutions of the crack widths on the surfaces of concrete obtained from the 2D models based on the assumption of a plane stress state and the corresponding cross-sections of the 3D model.

6 CONCLUSION

Based on the results of the presented study, the following conclusions regarding

the potential and the limitations of 2D mesoscopic modeling techniques for the simulation of cracking of concrete resulting from rebar corrosion are drawn:

• 2D mesoscopic simulation models deliver distributions of the current density around the rebar surface, the inward corrosion penetration, and the outward movement of the steel-concrete interface, which agree reasonably well for engineering purposes with the results obtained in corresponding cross-sections of an underlying 3D mesoscopic simulation model.

• All three types of physical quantities are influenced by the aggregates in the immediate vicinity of the rebar. Since the aggregate arrangement varies along the axial direction of the rebar, the three types of physical quantities also vary significantly in that direction. Thus, it is recommended to perform *several* 2D simulations with *different* realistic aggregate arrangements in order to get insight into the described variabilities along the axis of the rebar.

• It was shown that 2D mesoscopic models do not necessarily reproduce the interaction of propagating cracks with the aggregates. This has the potential to lead to qualitatively and quantitatively incorrect predictions of crack propagation paths and evolutions of crack opening widths. For a high level of reliability, 3D mesoscopic simulations appear to be indispensable.

• The assumptions of a plane strain state or a plane stress state do not have a significant effect on the simulation results of 2D mesoscopic models.

ACKNOWLEDGMENTS

Financial support from the China Scholarship Council (Grant number 202206260161) and the China Association for Science and Technology (Outstanding Chinese and Foreign Youth Exchange Program, Grant number 0200151002) is gratefully acknowledged.

REFERENCES

[1] Alexander Michel, Brad J Pease, Mette R Geiker, Henrik Stang, and John Forbes Olesen. Monitoring reinforcement corrosion and corrosion-induced cracking using non-destructive X-ray attenuation measurements. *Cement and Concrete Research*, 41(11):1085–1094, 2011.

[2] Filipe Pedrosa and Carmen Andrade. Corrosion induced cracking: Effect of different corrosion rates on crack width evolution. *Construction and Building Materials*, 133:525–533, 2017.

[3] Evžen Korec, Milan Jirásek, Hong S Wong, and Emilio Martínez-Pañeda. A phase-field chemo-mechanical model for corrosion-induced cracking in reinforced concrete. *Construction and Building Materials*, 393:131964, 2023.

[4] Licheng Wang, Yongqin Liang, and Tamon Ueda. Numerical simulation of corrosion-induced cracking of concrete considering rust penetration into cracks. *Journal of Materials in Civil Engineering*, 33(8):04021183, 2021.

[5] Yue Li, Xin Ruan, Herbert Mang, and Bernhard Pichler. 3D mesoscopic analysis of counterintuitive cracking of concrete in an accelerated rebar corrosion test. Under review, 2024.

[6] C Andrade, C Alonso, and FJ Molina. Cover cracking as a function of bar corrosion: Part I – Experimental test. *Materials and Structures*, 26:453–464, 1993.

[7] Markus Königsberger, Bernhard Pichler, and Christian Hellmich. Micromechanics of ITZ–aggregate interaction in concrete: Part I – stress concentration. *Journal of the American Ceramic Society*, 97(2):535–542, 2014.

[8] Markus Königsberger, Bernhard Pichler, and Christian Hellmich. Micromechanics of ITZ–aggregate interaction in concrete: Part II – strength upscaling. *Journal of the American Ceramic Society*, 97(2):543–551, 2014.

[9] Xurui Fang, Zichao Pan, Airong Chen, Hao Tian, and Rujin Ma. Phase-field method for modeling non-uniform corrosion-induced cracking in concrete. *Engineering Fracture Mechanics*, 281:109131, 2023.

[10] Branko Šavija, Mladena Luković, José Pacheco, and Erik Schlangen. Cracking of the concrete cover due to reinforcement corrosion: A two-dimensional lattice model study. *Construction and Building Materials*, 44:626–638, 2013.

[11] Bernhard Elsener. Macrocell corrosion of steel in concrete – implications for corrosion monitoring. *Cement and Concrete Composites*, 24(1):65–72, 2002.

[12] Kolluru V Subramaniam and Mingdong Bi. Investigation of steel corrosion in cracked concrete: Evaluation of macrocell and microcell rates using tafel polarization response. *Corrosion Science*, 52(8):2725–2735, 2010.

[13] SC Kranc and Alberto A Sagüés. Detailed modeling of corrosion macrocells on steel reinforcing in concrete. *Corrosion Science*, 43(7):1355–1372, 2001.

[14] Jesse P Angle, Zhaojie Wang, Chris Dames, and Martha L Mecartney. Comparison of two-phase thermal conductivity models with experiments on dilute ceramic composites. *Journal of the American Ceramic Society*, 96(9):2935–2942, 2013.

[15] KK Sagoe-Crentsil and Fredrick P Glasser. "Green rust", iron solubility and the role of chloride in the corrosion of steel at high pH. *Cement and Concrete Research*, 23(4):785–791, 1993.

[16] Alexander Michel, Brad J. Pease, Adéla Peterová, Mette R. Geiker, Henrik Stang, and Anna Emilie A. Thybo. Penetration of corrosion products and corrosion-induced cracking in reinforced cementitious materials: Experimental investigations and numerical simulations. *Cement and Concrete Composites*, 47:75–86, 2014.

[17] Sabine Caré, Quang Thanh Nguyen, Valérie L'Hostis, and Yves Berthaud. Mechanical properties of the rust layer induced by impressed current method in reinforced mortar. *Cement and Concrete Research*, 38(8-9):1079–1091, 2008.

[18] A Goldman and A Bentur. Effects of pozzolanic and non-reactive microfillers on the transition zone in high strength concretes. In *RILEM Proceedings*, pages 53–53. CHAPMAN & HALL, 1992.

[19] Hasan M Albegmprli, Abdulkadir Cevik, M Eren Gulsan, and Ahmet Emin Kurtoglu. Reliability analysis of reinforced concrete haunched beams shear capacity based on stochastic nonlinear FE analysis. *Computers and Concrete*, 15(2):259–277, 2015.

[20] Jan G Rots, P Nauta, GMA Kuster, and Johan Blaauwendraad. Smeared crack approach and fracture localization in concrete. *HERON, 30 (1), 1985*, 1985.

[21] Congjie Wei, Charles S Wojnar, and Chenglin Wu. Hydro-chemo-mechanical phase field formulation for corrosion induced cracking in reinforced concrete. *Cement and Concrete Research*, 144:106404, 2021.